Green Chemistry

PAPER

View Article Online
View Journal | View Issue

Check for updates

Cite this: *Green Chem.*, 2024, **26**, 11259

Biomass-derived polyol esters as sustainable phase change materials for renewable energy storage†

Magdalena Gwóźdź, [a] Marta Markiewicz, [b] Stefan Stolte, [b] Anna Chrobok, [a] David R. Turner, [c] Karolina Matuszek *[c] and Alina Brzęczek-Szafran *[a]

Received 15th July 2024,
Accepted 16th September 2024

DOI: 10.1039/d4gc03460k

rsc.li/greenchem

Innovative thermal battery technology has the capability to revolutionize the renewable energy storage market. Its cost-effectiveness, scalability, contribution to CO_2 reduction, and lack of reliance on rare earth metals set it apart. Nevertheless, the overall efficiency and sustainability of this technology hinge on crucial factors such as the sources, performance, and cost of the associated phase-change material (PCM). Fatty acid esters with biorenewable origins meet the sustainability criteria yet are limited to low-temperature applications (mostly <70 °C). In this study, we explored a new strategy to fine-tune the operating temperature of esters by adding hydroxyl groups, which are capable of forming H-bonds, positively affecting crystal packing and boosting their thermal properties. OH-group-rich, and biorenewable tartaric and mucic acids were employed as the core of fatty acid esters. Combinations of tartaric acid and fatty alcohols gave sustainable PCMs (confirmed by green chemistry metrics) with high melting enthalpies up to 221 J g^{-1}, improved melting temperatures up to 94 °C, and high stability demonstrated over more than 500 cycles. With the aid of Fourier-transform infrared spectroscopy (FTIR), synchrotron single-crystal X-ray diffraction, and Hirshfeld surface analyses, we obtained insights into the molecular interactions dictating the extraordinary thermal properties of sugar acid-derived esters, which could be feasible as PCMs for sustainable and inexpensive energy storage.

Open Access Article. Published on 11 Oktober 2024. Downloaded on 07.01.26 22:54:55.
This article is licensed under a Creative Commons Attribution 3.0 Unported Licence.

Introduction

Thermal energy storage (TES) is a valuable solution for mitigating the energy crisis by efficiently storing surplus thermal energy and thus easing strain on the power grid.[1] Taking into consideration the intensified actions undertaken globally to achieve carbon neutrality, which the EU has committed to achieve by 2050,[2] TES has the potential to play a dual role in shaping a more sustainable future:[3–6] firstly, by contributing to energy supply and, secondly, by reducing CO_2 emissions through minimizing the reliance on fossil fuel-based power generation.[7] To fully address the sustainability of these inexpensive, easily scalable technologies, the materials involved cannot be neglected, *i.e.*, their source, performance, price, and utilization/circularity should be considered.[8] Phase-change materials (PCMs) have significant potential in TES applications. PCMs harness latent heat during a phase transition, typically solid–liquid, with the operating temperature defined by the melting temperature (T_m) and the energy storage capacity determined by the enthalpy of fusion (ΔH_f).[9] PCMs should possess a high TES density, undergo reversible crystallization/melting within narrow temperature ranges, and maintain high thermal stability.[1] To be fully sustainable, they should also be environmentally acceptable, *i.e.*, show high biodegradability and low toxicity. Current research focuses on organic PCMs, which, in comparison with inorganic PCMs, are less corrosive, exhibit lower supercooling, and do not suffer from phase separation. The operating temperature range of organic PCMs is suitable for applications in TES,[10–12] utilized in, *e.g.*, thermo-regulated textiles,[13] solar air heaters,[14] solar stills,[15] solar hot water systems,[16] or the heating and cooling of buildings.[17–19]

As organic materials for low/medium temperature applications, paraffins have been recognized as having superior properties, such as high heat capacity, chemical inertness, little supercooling, little volume change during melting, and, additionally, low cost. Unfortunately, their production from crude oil contributes to CO_2 emissions and fossil fuel depletion.[12,20] Greener alternatives are fatty acids and alcohols, both of which show high enthalpies of phase transitions

[a]*Silesian University of Technology, Faculty of Chemistry, Gliwice, Poland. E-mail: alina.brzeczek-szafran@polsl.pl*
[b]*Institute of Water Chemistry, Dresden University of Technology, Bergstrasse 66, D-01069 Dresden, Germany*
[c]*Monash University, School of Chemistry, Melbourne, Australia. E-mail: karolina.matuszek@monash.edu*

†Electronic supplementary information (ESI) available. CCDC 2369962 and 2369963. For ESI and crystallographic data in CIF or other electronic format see DOI: https://doi.org/10.1039/d4gc03460k

Open Access Article. Published on 11 Oktober 2024. Downloaded on 07.01.26 22:54:55.
This article is licensed under a Creative Commons Attribution 3.0 Unported Licence.

(ranging from 45 to approximately 250 J g^{-1}), high thermal stability, and T_m ranging from −5 °C to 71 °C, and additionally show no significant supercooling.[21–23] They can be obtained from sources such as plant oils, ensuring availability, material circularity, and low cost.[24] Modifying the fatty acid/alcohol chain allows the thermal properties to be modified, *e.g.*, longer alkyl chains offer greater degrees of freedom in the liquid phase, leading to increased melting entropy (ΔS_f).[3] Additionally, they tend to form stronger intermolecular bonds and tighter crystalline structures, necessitating higher temperatures for bond-breaking and ultimately influencing the phase transition temperature and the latent heat of fatty acids.[7,21,24,25] Nevertheless, the drawbacks of fatty acids are corrosiveness, unpleasant odor, sublimation during heating, and flammability. On the other hand, a solid–solid transition prior to melting has been identified for fatty alcohols. This transition has the potential to mitigate the released thermal energy under specific circumstances.[26,27]

A promising solution to overcome these limitations is the derivatization of fatty acids with alcohols to give esters. Fatty acid esters lack the bad odor, exhibit high thermal stability, higher T_m relative to paraffins and fatty acids, and no corrosiveness.[28–30] Moreover, this group of PCMs is present in the portfolio of companies offering PCMs,[31] manifesting their commercial potential. Nevertheless, their T_m values, which are mostly <70 °C, make them desirable PCMs only for low/medium temperatures.

In initial studies, fatty acid esters obtained by the esterification of stearic and palmitic acids with alcohols (methanol, propanol, or butanol) were studied.[32] The resulting esters showed T_m in the range of 17–34 °C, with methyl stearate demonstrating the highest ΔH_f of 199 J g^{-1}. With an increase in the alcohol's carbon chain length, ΔH_f decreased, while T_m showed an opposite trend. Floros and Narine[20] proposed a solvent-free synthesis of diesters derived from fatty acid esters (methyl stearate, methyl palmitate, methyl myristate, and methyl laurate) and a linear diol (ethylene glycol-1,10-decanediol). These fatty esters exhibited T_m ranging from 39 to 77 °C and possessed a remarkably high heat capacity of up to 260 J g^{-1} for ethane-1,2-diyl dipalmitate, which is the highest known enthalpy among all diesters. Aydin *et al.*,[33–35] Sari *et al.*,[36] Stamatiou *et al.*,[37] Özlem Kaplan *et al.*,[38] and Ravotti *et al.*[28,39] explored a wide series of linear esters synthesized by reacting fatty acids with diols, diacids with fatty alcohols, or glycerin with fatty acids. These materials exhibited high ΔH_f (150–226 J g^{-1}) and a wide range of T_m (10–60 °C). Furthermore, abundant, benign, inexpensive sugar alcohols that show high melting enthalpy (even up to 330 J g^{-1} for galactitol)[40–43] have been used as precursors for the synthesis of esters, which were examined as PCMs. Sari *et al.* esterified glycerol,[44] erythritol,[45] xylitol,[46] mannitol,[47] and galactitol[48] with fatty acids (stearic, palmitic, myristic, and lauric acid), resulting in a series of tri-, tetra-, penta-, and hexa-esters that exhibited low T_m values (22–65 °C) and high melting enthalpies (145–251 J g^{-1}), with the highest reported being for galactitol hexastearate. Even though the sugar alcohols used as starting materials are rich in hydroxyl groups (which are capable of forming strong H-bonds), the strategy applied was focused on their quantitative esterification with fatty acids, leading to no free groups being left.

The high enthalpies of fusion of esters resulted from the intramolecular van der Waals interactions between their $-CH_2-$ units.[49] Not surprisingly, initial research was primarily focused on the impact of the hydrocarbon chain length and overall molecular arrangement on the changes in ΔH_f and T_m. However, as some authors of this study have shown, H-bonding interactions can also fine-tune the thermal properties of organic PCMs, leading to increased ΔH_f values[6,50,53] observed also by other groups.[51,52,54]

Existing PCMs for applications above 70 °C, such as sterilization, are primarily fossil fuel-derived paraffins and amides, while sustainable fatty acids, fatty alcohols, or esters mostly melt at lower temperatures. The state of the art for existing organic PCMs in this temperature range is summarized in Table 6, ESI.†

Driven by the need for sustainability and material circularity, inexpensive, biomass-derived tartaric acid (TA) or mucic acid (MA) were employed as the cores of fatty acid esters, which were capable of forming H-bonds. By varying the number of hydroxyl groups in the core of fatty acid esters and the length of their alkyl chains, structure–property relationships, which were studied by temperature-dependent FT-IR analysis, crystallographic analysis, and Hirshfeld surface analysis, were elucidated, aiming to uncover a way to design highly efficient, sustainable PCMs with tunable operating temperature ranges.[39] Additionally, the biodegradability of these materials was studied as a key property influencing their environmental impact.

Experimental

The ESI† section provides a detailed account of the synthesis of tartaric acid diesters, including comprehensive characterization data and a thorough list of the materials used.

Materials

The long-chain sugar acid esters were synthesized using L-(+)-tartaric acid (>99.5%), mucic acid (>99%), 1-dodecanol (>98%), 1-hexadecanol (>99%), 1-octadecanol (>99%), and 1-docosanol (>99%) obtained from Sigma-Aldrich. The reaction also used Amberlyst™-15 or *p*-toluenesulfonic acid as catalysts (Merck). Ethanol (>99%) was used for crystallization to purify the final products. All reagents were used without purification.

Characterization

Nuclear magnetic resonance. The structures were confirmed by ^{1}H NMR and ^{13}C NMR (SI), using a 400 MHz Agilent spectrometer. Chemical shifts (ppm) were reported relative to the internal standard tetramethylsilane, with $CDCl_3$ and *d*6-DMSO as the solvents.

Mass spectrometry. High-resolution mass spectrometry analyses were conducted using a Waters Xevo G2 QTof mass

 This journal is © The Royal Society of Chemistry 2024

Open Access Article. Published on 11 Oktober 2024. Downloaded on 07.01.26 22:54:55.
This article is licensed under a Creative Commons Attribution 3.0 Unported Licence.

spectrometer with an ESI source operating in positive-ion mode. MassLynx software was employed to accurately determine the mass and composition of the molecular structure.

Thermogravimetric analysis (TGA). TGA was carried out on a Mettler Toledo TGA/DSC 1 STARe system. The samples (3 mg to 10 mg) were securely enclosed in hermetically sealed aluminum pans. A heating rate of 10 °C min^{-1} was applied, raising the temperature from 25 to 550 °C. Throughout the experiments, a nitrogen flow of 30 mL min^{-1} was maintained.

Differential scanning calorimetry (DSC). Phase transition temperatures, such as melting and freezing temperatures, and the associated heat of fusion (ΔH_f), were measured using a TA Q200 differential scanning calorimeter (TA Instruments), which was calibrated with indium (TA Instruments, T_m = 156 °C, ΔH_f = 28.45 J g^{-1}) and cyclohexane (Sigma-Aldrich, T_m = 8 °C) standards. The DSC measurements were conducted in triplicate under a nitrogen atmosphere, with sample sizes ranging from 2 to 7 mg and a heating rate of 10 °C min^{-1}. The values employed were taken from the second run of the heating and cooling cycle for stable compounds and from the first run for compounds that decomposed. The peak maximum was used to determine the melting point (T_m) and crystallization temperature (T_c), while ΔH_f was calculated based on the area under the melting peak (using Pyris software for integration under the endothermic transition peak). T_m was consistently chosen as the peak maximum in order to ensure reliability throughout the study.

Fourier-transform infrared spectroscopy (FT-IR). Transmission FT-IR spectra for the prepared samples of TA and MA diesters were recorded at room temperature (RT) and after melting using a Mettler Toledo iC10 Fourier transform IR spectrometer, equipped with a liquid-nitrogen-cooled mercury-cadmium-telluride detector. The samples were pressed onto a diamond ATR crystal. All data were collected before and after melting the diesters, within a range of 4000–650 cm^{-1}, at a resolution of 2 cm^{-1}, and averaged over 64 scans.

Crystallography. Data for C_{12}_TA_C_{12} and C_{18}_TA_C_{18} were collected on the Micro Crystallography – MX2 beamline at the Australian Synchrotron,[55] at 100 K. Data collection and integration were performed using the Blu-Ice[56] and XDS software programs.[57] The diester structures were solved and refined using the SHELX[58,59] software suite and refined against F^2 using Olex2.[60] Non-hydrogen atoms were refined with anisotropic displacement parameters, and hydrogen atoms attached to carbon were included in the calculated positions. O–H protons were modelled based on electron density. In C_{18}_TA_C_{18}, O–H protons were modelled as disordered over two positions, with a fixed occupancy of 0.5. The C_{12}_TA_C_{12} and C_{18}_TA_C_{18} crystals were grown from a saturated ethyl acetate/ethanol mixture using a monowave, followed by slow-cooling.

Biodegradation. The biodegradability was screened using the OECD guideline 301-F[61] ready biodegradability test using an OxiTop® test system (WTW, Weilheim, Germany). The test was conducted in an OECD medium containing the test compound, a nitrification inhibitor (allylthiourea, 5 mg L^{-1}), and microbial inoculum. The effluent from the aeration tank of a municipal WWTP in Dresden, Germany, was preconditioned by aeration for 3 days and used as the inoculum source. The inoculum was spiked into respirometers to achieve a final concentration of 30 mg of total suspended solid per L. The number of live aerobic bacteria was established to be 105 colony forming units per L by using agar dip slides (Lovibond, Dortmund, Germany). The test compounds were added to respirometers as solids to yield a theoretical oxygen demand (ThOD) of 40 mg O2 per L (corresponding to a concentration of approximately 15 mg L^{-1}). Two or three replicates were run for each test substance, accompanied by three blank samples to account for internal cellular respiration and two positive controls containing sodium benzoate. The tests were run for 28 days under constant stirring at 20 ± 1 °C in amber glass bottles.

Toxic inhibition of inoculum. The test was conducted in the same manner as the biodegradability test described above, except easily biodegradable sodium benzoate was also added to each respirometer (except blanks) in the same concentration as used in the positive control bottles. Lower or delayed biodegradability of sodium benzoate in the presence of the test compound was interpreted as a sign of toxicity toward inoculum. Toxic inhibition of inoculum activity was tested at two concentrations of tartaric and mucic acid diesters: approximately 15 mg L^{-1} (concentration used in the biodegradation test) and 4 mg L^{-1} (only for homologs containing alkyl chains longer than 18 carbons).

Results and discussion

Synthesis

Two groups of diesters were synthesized by using L-(+)-tartaric acid or mucic acid as precursors with a different number of hydroxyl groups (two or four, respectively). The esters of L-(+)-tartaric acid were synthesized through a straightforward procedure by esterification with fatty alcohols (1-dodecanol, 1-hexadecanol, 1-octadecanol, or 1-docosanol) (Fig. 1). In turn, the high polarity of mucic acid and the resulting difficulty in contacting non-polar fatty alcohols hindered direct esterification. Therefore, mucic acid was first transformed into mucic acid dibutyl ester, which was further reacted with fatty alcohols.

The chosen hydroxyl-group-rich precursors are readily available, fully biobased, and sustainable. Tartaric acid is a naturally occurring organic acid that can be found in various fruits, including grapes, apples, and tamarind.[62] It can be naturally sourced through the acid hydrolysis of calcium tartrate, which is derived from potassium tartrate obtained as a byproduct in winemaking[62,63] or synthesized from maleic anhydride.[64] Likewise, mucic acid is sourced from fruit, as well as from sugar beet.[65] It can be produced by oxidation of galactose,[66] electrolytic oxidation of D-galacturonate,[67] or microbial conversion of D-galacturonate.[66,68,69] Valorization of wastes from wine production or the dairy industry not only promotes sustainable

Open Access Article. Published on 11 Oktober 2024. Downloaded on 07.01.26 22:54:55.
This article is licensed under a Creative Commons Attribution 3.0 Unported Licence.

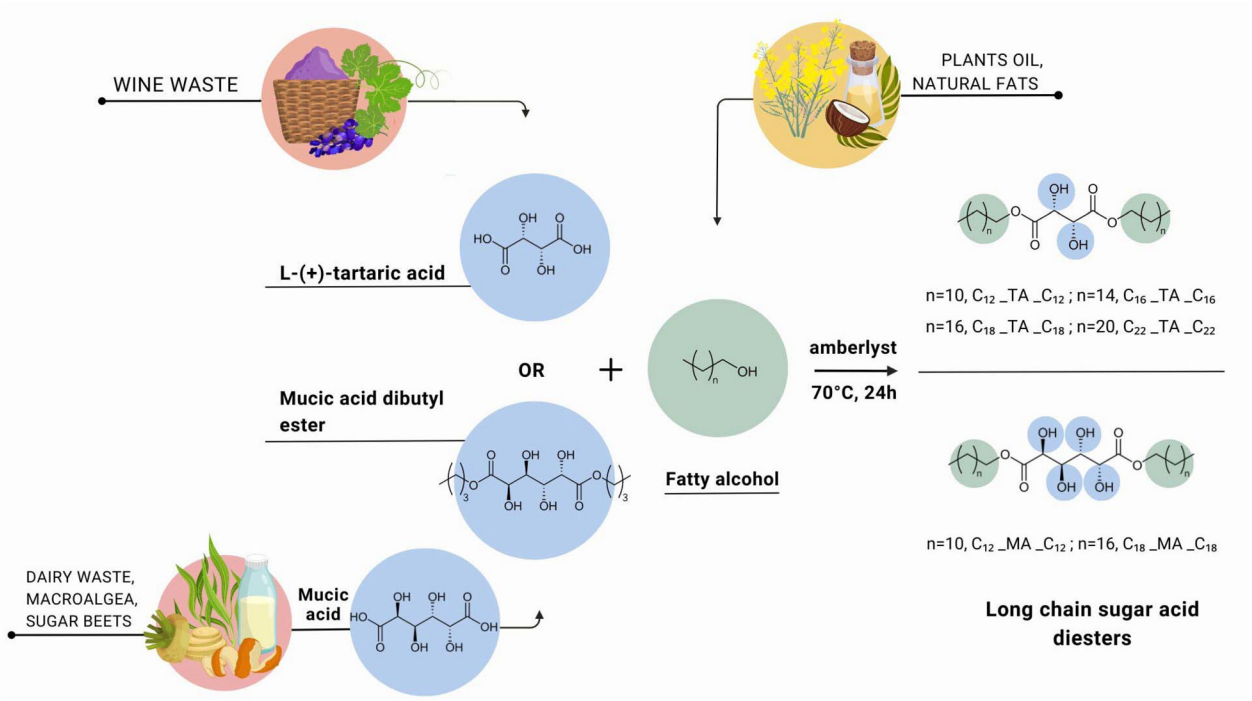

Fig. 1 Scheme of synthesis of long-chain tartaric acid diesters (C_{12}_TA_C_{12}, C_{16}_TA_C_{16}, C_{18}_TA_C_{18}, and C_{22}_TA_C_{22}) and mucic acid diesters (C_{12}_MA_C_{12} and C_{18}_MA_C_{18}).

resource management and the circular economy, but also does not deplete food resources.[70] On the other hand, fatty alcohols are crucial compounds sourced from natural fats and oils from plants, animals, and microorganisms.[71] They can be derived from fatty acids found in coconut oil, obtained through the hydrogenation[72] of other vegetable oils or produced by the conversion of petroleum feedstock.[71]

In addition to the source of the precursors, the synthetic procedure applied for diesters was evaluated and analyzed according to green chemistry principles using J. Clark's Green Chemistry metrics toolkit (Appendix 1, ESI†)[73] to fully assess its sustainability. All key reaction conditions (reaction temperature, time, catalysts, and purification method) were carefully selected to best adhere to green chemistry parameters as discussed below for a representative tartaric acid derivative (C_{18}_TA_C_{18}), which was used due to its high potential as a sustainable PCM, as discussed in further sections.

The precursor (TA) was transformed into the desired product with high conversion (>99%) and a selectivity of 70% toward diesters (marked with an amber flag), giving a yield of 70% (marked with an amber flag). Nevertheless, stearyl alcohol was used in excess, contributing to a reaction mass efficiency (RME) of 29%. The synthesis was performed solventless (green flag), bolstering the PMI, which could be marked with a green flag. The esterification reaction was conducted with a heterogeneous, reusable catalyst (Amberlyst-15), which could be assigned a green flag; at 70 °C, this translates into a green flag with regard to the energy consumption parameter. The synthesis was conducted in batch mode (amber flag), but potentially it could be performed under continuous flow conditions with a heterogeneous catalyst. The product was purified by crystallization from ethanol, which means that the work-up procedure could be assigned a green flag. Finally, the synthesis included no critical elements (green flag) and no chemicals with H-codes regarding their health and safety parameters. Although full optimization of the synthetic method is beyond the scope of this study (future work should focus on optimization of the reactant ratio and related selectivity toward diesters), the synthesis of tartaric acid esters has full sustainable potential with little environmental impact.

Thermal properties

Thermophysical properties play a significant role in assessing a material's capacity to efficiently store and release thermal energy, thus defining its potential applications. Diesters of tartaric and mucic acids were characterized in terms of their melting temperature (T_m), enthalpy of fusion (ΔH_f), crystallization temperature (T_c), enthalpy of crystallization. (ΔH_c), and supercooling temperature ($\Delta T = T_m - T_c$) using DSC. Thermal stability was investigated using TGA analysis, and the entropy of fusion (ΔS_f) was calculated using the Gibbs equation based on the T_m and ΔH_f data. The results are presented in Table 1. Both TA and MA decompose upon melting at 172 °C and 205 °C, respectively, which excludes them from TES applications in their pristine form. However, the esterification of TA with fatty alcohols gave products with T_m values ranging from 67 to 94 °C ± 2 °C and ΔH_f values ranging from 133 to 221 J g^{-1} ± 5%. These values of T_m are comparable to those exhibi-

 This journal is © The Royal Society of Chemistry 2024

Open Access Article. Published on 11 Oktober 2024. Downloaded on 07.01.26 22:54:55.
This article is licensed under a Creative Commons Attribution 3.0 Unported Licence.

Table 1 Physical properties of tartaric acid diesters (C_{12}_TA_C_{12}, C_{16}_TA_C_{16}, C_{18}_TA_C_{18}, and C_{22}_TA_C_{22}), mucic acid diesters (C_{12}_MA_C_{12} and C_{18}_MA_C_{18}) and their precursors, TA and MA

Compound	T_m [°C] ± 2 °C	ΔH_f [J g^{-1}] ± 5%	T_c [°C] ± 2 °C	ΔH_c [J g^{-1}] ± 5%	ΔS_f [J mol^{-1} K^{-1}]	T_d [°C]
TA	D	—	—	—	—	172
C_{12}_TA_C_{12}	67	133	51	132	190	288
C_{16}_TA_C_{16}	77	162	60	169	277	286
C_{18}_TA_C_{18}	82	221	71	218	408	297
C_{22}_TA_C_{22}	94	203	80	201	424	289
MA	D	—	—	—	—	205
C_{12}_MA_C_{12}	137	205[a]	—	—	—	150
C_{18}_MA_C_{18}	124	194[a]	—	—	—	169

[a] ΔH_f taken from the 1st heating cycle due to the decomposition in the second cycle. D – decomposition.

ted by monoamides[74] and triglycerides.[75] In the series of tartaric acid esters, the increase in the alkyl chain length increased the T_m, reaching 94 °C ± 2 °C for C_{22}_TA_C_{22} (Fig. 2). This trend can be attributed to stronger intermolecular interactions formed by longer carbon chains.[4] As the carbon chain length increases in a series of compounds (*e.g.* alkanes or fatty acids),[76] an increase in the melting temperature and enthalpy of fusion is observed due to stronger van der Waals interactions between molecules and stronger instantaneous dipol-induced dipol interactions. Longer chains can align and pack more efficiently in the solid state, creating a more ordered structure. The greater order in the solid state means a larger entropy increase upon melting, contributing to a higher enthalpy of melting. Therefore, with the increase in the alkyl chain length from C_{12}_TA_C_{12} to C_{18}_TA_C_{18}, ΔH_f values increased, reaching 221 J g^{-1} ± 5% for C_{18}_TA_C_{18}.

In the series of tartaric acid diesters, the ΔH_f is lower than that for the pure paraffins (C12: 215 J g^{-1}; C16: 235 J g^{-1}; C18: 237 J g^{-1}; and C22: 249 J g^{-1}). Meanwhile, in the literature, it is observed that an increasing number of hydroxyl groups leads to higher melting temperatures and enthalpies, due to more hydrogen bonding that creates a more rigid and ordered structure in the solid state.[77] In this case, the two factors counteract each other: (i) longer chains increase hydrophobicity, which can reduce the effectiveness of hydrogen bonding in some cases; (ii) the placement of hydroxyl groups along the carbon chain can affect how easily the molecules can pack in the solid state.

This can also explain why the elongation of the alkyl chain to C_{22} decreased the ΔH_f to 203 J g^{-1} ± 5%, which can be most probably ascribed to the weakening of the hydrogen bonds,[74] as well as van der Waals interactions, simultaneously contributing to lower ΔH_f values.

Moreover, the melting peak of C_{22}_TA_C_{22} displayed heterogeneity in the thermogram registered at 10 °C min^{-1} (Fig. 2), suggesting possible polymorphism, common for systems with lengthy alkyl chains.[75] Nevertheless, when heated at a rate of 1 °C min^{-1}, only one melting transition was observed (Fig. S23†). The melting peak became noticeably narrower, leading to a slight reduction in T_m, which is a typical outcome observed at lower heating rates.[78]

Comparing T_m and ΔH_f values for the investigated hydroxyl group-rich diester of stearyl alcohol and tartaric acid (ΔH_f of 221 J g^{-1} ± 5% and T_m = 82 °C ± 2 °C) and a similar diester without hydroxyl groups (the ester of stearyl alcohol and succinic acid; ΔH_f of 194 J g^{-1} ± 5% and T_m = 64 °C ± 2 °C), a significant role of hydrogen bonds in shifting T_m and ΔH_f toward increased values was observed.

To further investigate the influence of the hydroxyl groups on the thermal properties of fatty esters, the tartaric acid core was replaced with mucic acid.[79] Increasing the number of hydroxyl groups in the system and, therefore, possibly obtaining more robust hydrogen bonding interactions led to higher T_m values of the resulting esters (from 124 to 137 °C ± 2 °C) than those reported for the series based on tartaric acid (from 67 to 94 °C ± 2 °C). Intriguingly, in contrast to tartaric acid esters, the T_m and ΔH_f values decreased with the increase in the alkyl chain length. A similar observation was reported for the ΔH_f values of behenic acid monoesters.[80] It was found that a larger number of hydroxyl groups could disturb the intermolecular packing of the alkyl chains and thus weaken the van der Waals interactions, resulting in decreased ΔH_f, and this topic is further discussed in the Crystallography section.

The high thermal stability of the investigated tartaric acid esters, ranging from 286 °C for C_{16}_TA_C_{16} to 297 °C for C_{18}_TA_C_{18}, which is well above their maximum working temperature (defined as T_m + 10°),[9] indicates their high potential for practical applications (Fig. 3a). The elongation of the alkyl chain in both the TA- and MA-derived series from C_{12} to C_{18} led to an increase in the decomposition temperature from 288 °C for C_{12}_TA_C_{12} to 297 °C for C_{18}_TA_C_{18} and from 150 °C for C_{12}_MA_C_{12} to 169 °C for C_{18}_MA_C_{18}. On the other hand, the incorporation of two additional hydroxyl groups into the system led to a marked reduction in thermal

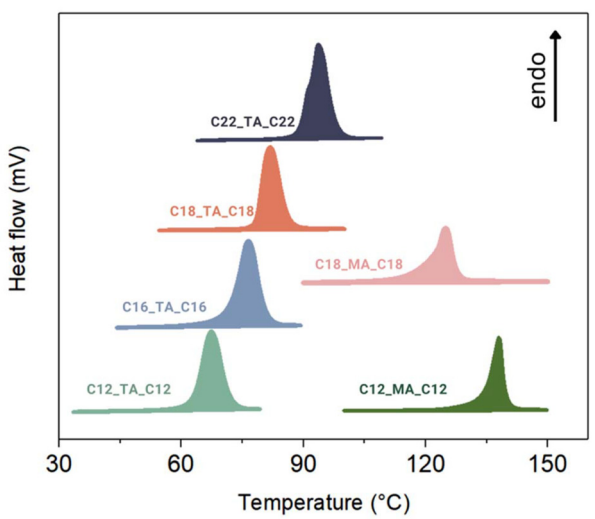

Fig. 2 DSC traces showing the second heating cycle for the tartaric acid diesters (C_{12}_TA_C_{12}, C_{16}_TA_C_{16}, C_{18}_TA_C_{18}, and C_{22}_TA_C_{22}) and the first heating cycle of the mucic acid diesters (C_{12}_MA_C_{12} and C_{18}_MA_C_{18}), at a ramp rate of 10 °C min^{-1}.

Open Access Article. Published on 11 Oktober 2024. Downloaded on 07.01.26 22:54:55.
This article is licensed under a Creative Commons Attribution 3.0 Unported Licence.

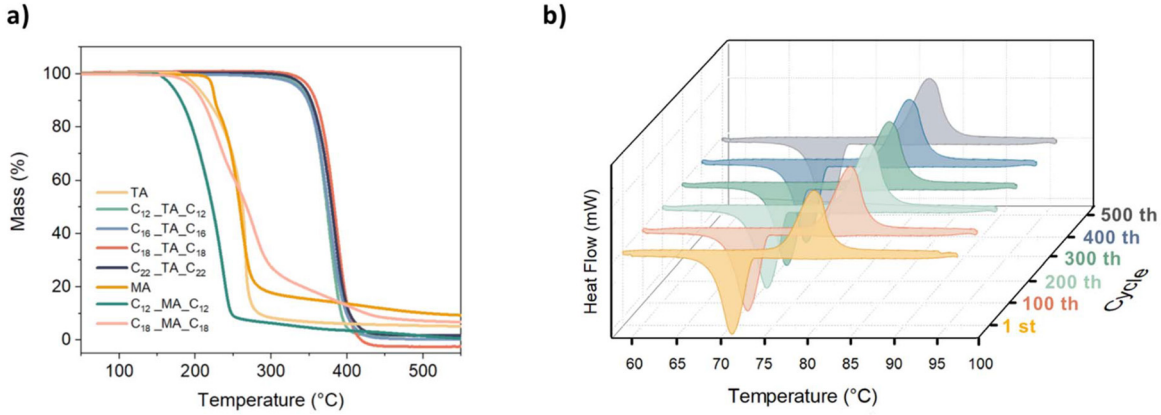

Fig. 3 (a) TGA curves of tartaric acid (C_{12}_TA_C_{12}, C_{16}_TA_C_{16}, C_{18}_TA_C_{18}, and C_{22}_TA_C_{22}), mucic acid diester (C_{12}_MA_C_{12} and C_{18}_MA_C_{18}) and their precursors (TA and MA) at a 10 °C min^{-1} heating rate, and (b) latent heat values of C_{18}_TA_C_{18} after different thermal cycles, at a ramp rate of 10 °C min^{-1}.

stability from 288 °C for C_{12}_TA_C_{12} to 150 °C for C_{12}_MA_C_{12}. This finding underscores the importance of considering the relationship between possible van der Waals interactions and hydrogen bonding (whose effects can counteract each other) in the future design of sustainable PCMs. Most importantly, despite MA derivatives melting >120 °C with remarkable values of ΔH_f, they showed no repetitive phase transitions in a subsequent heating–cooling experiment, which was performed with DSC (Fig. S22†), manifesting their degradation and hindering their application in TES. In contrast, tartaric acid esters, with their finely tuned operating temperature ranging from 67 to 94 °C ± 2 °C and high storage capacity reaching up to 221 J g^{-1} ± 5% for C_{18}_TA_C_{18} (which melts at 82 °C ± 2 °C), showed no significant changes after being initially evaluated over three heating–cooling cycles (Fig. S21†).

To further confirm the stability of the C_{18}_TA_C_{18} diester under repetitive heating and cooling conditions, long-term cycling tests were performed for a 5.1 mg sample using DSC (Fig. 3b). C_{18}_TA_C_{18} was heated and cooled 500 times at 10 °C min^{-1}, in a temperature range of 60–95 °C. The excellent stability of the material was confirmed by no changes in the enthalpy of melting and little supercooling (11 °C). After 500 cycles, the melting peak maintained its original shape, and the T_m showed no deviation. Additional FT-IR and ^{1}H NMR spectra were recorded for the sample after 500 cycles (Fig. S11 and Fig. S26†) and evidenced no changes compared to spectra recorded before cycling, highlighting the potential of tartaric acid esters as promising PCMs with excellent stability during cycling.

Understanding the influence of hydrogen bonds on phase change behavior

The impact of hydrogen bonds on the phase transition behavior and heat storage in PCMs is a key aspect of their design. Hydrogen bonding interactions can either enhance or substantially degrade the thermal properties of PCMs, as discussed in a recent review by Y. Liu *et al.*[81] Interestingly, in the two series of compounds investigated in the present paper, both trends can be observed. To better understand the nature of these interactions and their influence on the thermal properties of the series of diesters, the next section presents detailed characterization of the molecular interactions occurring in both series, with a particular emphasis on hydrogen bonds.

FT-IR

Each atom or group of atoms in a molecule contributes to the total enthalpy of melting, depending on its size, dipole moment, ability to form hydrogen bonds, and the surrounding environment. The sum of these interactions is reflected in the T_m and enthalpy.[82] To better understand the influence of additional hydroxyl groups in the ester core on a material's thermal properties, we used FT-IR analysis, which offers a precise interpretation of the structural changes found during the phase transitions of the investigated diesters. The FT-IR spectra of the representative C_{18}_TA_C_{18} and the corresponding C_{12}_MA_C_{12} in the liquid and solid states are presented in Fig. 4.

Two peaks at 3484 cm^{-1} and 3290 cm^{-1} observed in the solid state of the tartaric diester confirmed the presence of hydrogen bonds formed by the hydroxyl groups. Typically, unbonded hydroxyl groups absorb infrared light at a higher wavenumber than that observed for the investigated esters (>3500 cm^{-1}).[83] After melting, only one peak at 3543 cm^{-1} was observed, indicating the disruption of the hydrogen bonds and the presence of free hydroxyl groups. This observation was confirmed by the redshifted bands corresponding to symmetric and antisymmetric $-CH_2$ stretching at 2852 cm^{-1} and 2919 cm^{-1} (shifted by 4–5 cm^{-1} and 5–7 cm^{-1}, respectively) observed after melting. These shifts are related to the disruption of the diester crystal packing after melting, indicating increased disorder and mobility of the hydrocarbon chain.[80,84] Furthermore, the carbonyl band, which is sensitive to the formation of hydrogen bonds, was analyzed.[85] In the solid state, symmetric and asymmetric C=O vibrational bands at

 This journal is © The Royal Society of Chemistry 2024

Open Access Article. Published on 11 Oktober 2024. Downloaded on 07.01.26 22:54:55.
This article is licensed under a Creative Commons Attribution 3.0 Unported Licence.

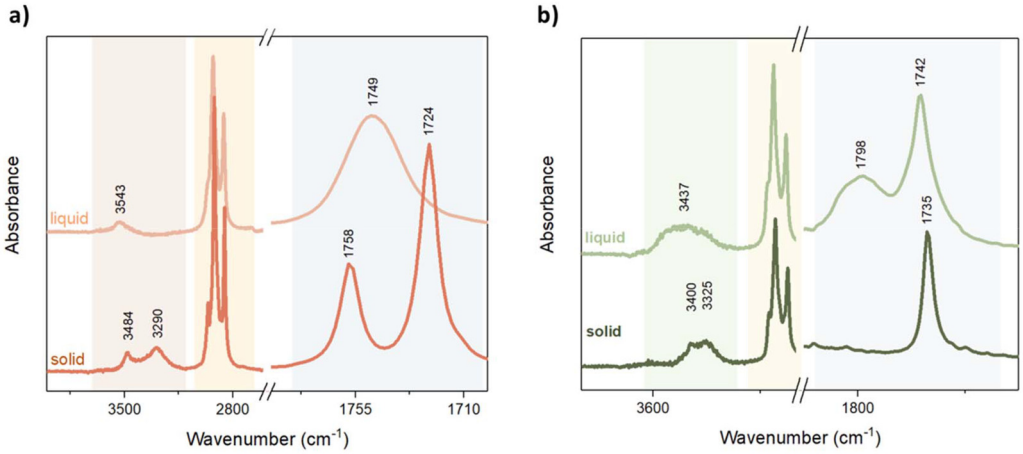

Fig. 4 The FTIR spectra of (a) C_{18}_TA_C_{18} and (b) C_{12}_MA_C_{12} collected at room temperature and after melting.

1724 cm^{-1} and 1758 cm^{-1}, respectively, were noticeable. As the temperature increased to the phase transition temperature, the hydrogen bonds broke, leading to a new vibrational band at 1749 cm^{-1}. The extension of the alkyl chains in tartaric acid diesters from C_{18}_TA_C_{18} to C_{22}_TA_C_{22} resulted in a weakening of the hydrogen bonds, as shown by a shift in the hydroxyl bands (from 3484 cm^{-1} and 3290 cm^{-1} to 3487 cm^{-1} and 3306 cm^{-1})[86] (Fig. 4a and Fig. S24†). These changes may explain the decrease in enthalpy with increasing chain length. Moreover, when the alkyl chain was extended to 22 carbon atoms, the largest increase in T_m in the series was observed.

For mucic acid diesters with four hydroxyl groups, the phase change occurred at a higher temperature, suggesting a robust network of hydrogen bonds that needed more energy to break. Similarly to the tartaric acid diester, the peaks corresponding to the hydroxyl groups at 3325 cm^{-1} and 3400 cm^{-1} disappeared during melting. Nevertheless, this time, they were replaced by a broad peak at 3437 cm^{-1} (Fig. 4b). Interestingly, in the spectrum of the solid C_{12}_MA_C_{12}, only one peak within the C═O bond region, at 1743 cm^{-1}, was observed. After melting, this peak remained mostly unchanged, but a new peak appeared at 1798 cm^{-1}, at a different position to the new peak found with the tartaric acid diester. It is worth noting that further analysis of the C_{12}_MA_C_{12} diester after recrystallization did not reveal the characteristic peaks of the original ester. Instead, the spectrum reflected that of the molten diester (Fig. S25†). This finding suggests decomposition/evaporation of C_{12}_MA_C_{12} after melting, even though the TGA showed no mass loss up to 220 °C (Fig. S17 and S18†). The peak formed at 1798 cm^{-1} and the broad band at 3437 cm^{-1} suggest that a mixture of diester and lactone was formed after melting. The ^{1}H NMR spectrum recorded after keeping the sample melted and stirred for 3 days further confirms the absence of –OH groups, as evidenced by the disappearance of their characteristic peaks (δ 4.82–4.63 and δ 3.75 (Fig. S12†)). Additionally, a slightly shifted peak at 4.5 ppm suggests the formation of a lactone. This is presumably caused by acid catalysis induced by water, as previously reported for other polyhydroxylated compounds. Some water is essentially always present in such hygroscopic polyhydroxylated compounds, which during prolonged high-temperature treatment can catalyze dehydration and cyclization reactions, shifting the equilibrium of H_2O towards H_3O^+ at 100 °C.[87] The degradation reaction is only observed during melting of mucic acid derivatives, which melt at higher temperature (124 and 137 °C) compared to the esters of tartaric acid (67–94 °C).

Crystallography

To gain further insight into the role of hydrogen bonding in the hydroxyl group-rich diesters, we investigated the crystal structures of the representative C_{12}_TA_C_{12} and C_{18}_TA_C_{18} obtained through single-crystal X-ray diffraction using synchrotron radiation on the best quality crystals available. It should be noted that determining the crystal structure of long-chain organic compounds from powder samples is often a labor-intensive process and not always feasible.[51] This was a problem we faced in this study, which limited the analysis to two materials and required synchrotron radiation. It was not possible to collect full data for C_{18}_TA_C_{18} but enough to unambiguously resolve the structure. C_{12}_TA_C_{12} crystallized in the monoclinic C2 space group with four molecules in a unit cell. Taking into consideration the hydroxyl groups' orientation, two out of the four molecules were directed toward each other with carbon chains arranged alternately in homologous, diagonal layers, parallel to the *bc* crystallographic plane (Fig. 5).

Adjacent chains from adjacent sheets were offset face-to-face, with an interplanar distance of 4.253 Å (C1–C1′ distance) (Fig. S29†). A similar molecular arrangement is observed in the structure of C_{18}_TA_C_{18}, which also crystallizes in the monoclinic C2 space group, with four molecules in the unit cell. Here, the interplanar distance is 4.010 Å (C40–C40′ distance), indicating denser packing in the C_{18}_TA_C_{18} crystal (Fig. S30†).

Open Access Article. Published on 11 Oktober 2024. Downloaded on 07.01.26 22:54:55.
This article is licensed under a Creative Commons Attribution 3.0 Unported Licence.

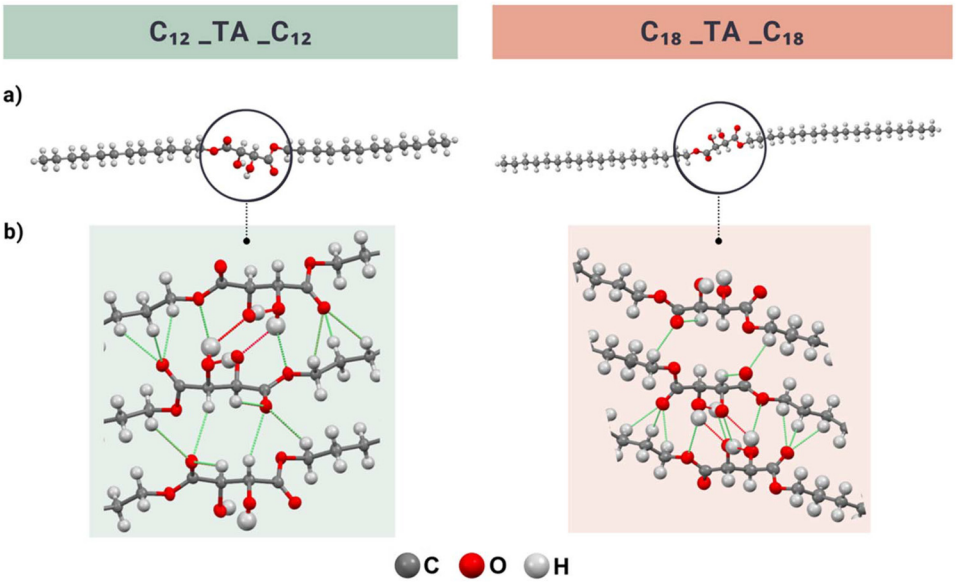

Fig. 5 (a) Lettice structure of C_{12}_TA_C_{12} and C_{18}_TA_C_{18} and (b) hydrogen bonding and core group interactions (red represents strong hydrogen bonds and green represents non-classical hydrogen bonds) in C_{12}_TA_C_{12} and C_{18}_TA_C_{18}, viewed down the *b* axis.

In the studied esters, hydrogen bonds typically vary in length from 2.6–3.0 Å (O–H···O); within this range, stronger hydrogen bonds tend to be shorter and have closer to linear angles.[88] In contrast to conventional hydrogen bonds, non-classical hydrogen bonds exhibit weaker strength and a longer distance between the donor and acceptor, extending up to ~3.5 Å.[89,90] These weak C–H···O bonds play a crucial role in stabilizing molecules, particularly in proteins, sugars, DNA, and crystal packing, having a significant impact on the thermal properties of materials.[91]

In the TA crystal structure, different types of hydrogen bonds were present, including shorter bonds (2.6–2.7 Å), formed by carboxylic acid hydrogens, and slightly longer bonds (2.8–2.9 Å), formed between the hydroxyl groups.[92] Both types of hydrogen bonds had O–H···O angles ≥165°, indicating their strong character. In turn, the C_{12}_TA_C_{12} molecule participated in four strong, conventional intermolecular hydrogen bonding interactions and several weaker, non-classical hydrogen bonds (Fig. 5, Tables S2 and S4†). Each hydroxyl group in the core acted as both a hydrogen bond donor and acceptor, forming connections with hydroxyl groups from two neighboring molecules. This configuration created an extensive network of hydrogen bonds formed by the tartaric acid-derived core of the adjacent molecules. In C_{12}_TA_C_{12}, the hydrogen bonds had similar lengths (O–H···O), ranging from 2.64 to 2.83 Å, but varied significantly in their angles. When the hydroxyl group acted as a donor, the bond angle was 174°, whereas when it acted as an acceptor, the angle was 126°. The notable presence of a considerable number of C–H···O bonds was particularly interesting. In the C_{12}_TA_C_{12} crystal, these bonds also formed between the oxygens of the carbonyl groups and the hydrogens of the alkyl groups nearest to the core or the hydrogen atoms of the hydroxyl group. They exhibited a length range of 3.07–3.55 Å, and the angles between the donor and acceptor ranged from 116–155°. Given the considerable length of the C–H···O bonds, the acceptor can be connected to two or three H atoms, resulting in bifurcated and trifurcated bonds.[90] In the C_{18}_TA_C_{18} molecule, a similar hydrogen bonding pattern is observed. Specifically, there are four strong hydrogen bonds with lengths ranging from 2.63 to 2.67 Å and angles from 123° to 168° (Fig. 5, Tables S3 and S4†). It was also observed that the hydrogen atom from the hydroxyl group forms both intramolecular and intermolecular hydrogen bonds, with a length of 3.07 Å and an angle of 114°.

The desired PCM should have enough strong hydrogen bonds in the crystalline phase to require a significant amount of energy to break them, resulting in efficient PCM loading. On the other hand, the H-bonds need to be capable of rearranging during the reverse process.[6] In the series of hydroxyl-group rich fatty esters, long symmetrical carbon chains and ester groups contribute to the flexibility of the molecule, facilitating the rearrangement of the crystal lattice upon crystallization.[3] Thus, the interplay between the hydrogen bonds and van der Waals interactions is crucial for ensuring both a high enthalpy of fusion and the stability of the PCM.

Hirshfeld surface analysis

The intermolecular interactions and their influence on crystal packing were further assessed using Hirshfeld surface analysis with CrystalExplorer software.[93] The analysis helps to visualize and quantify the interactions within a molecular crystal. The colors indicate the intensity and distance of contacts, where the normalized contact distance is based on the distance between the nuclei on the surface and the nearest nuclei outside the surface. The contacts at the van der Waals radius

 This journal is © The Royal Society of Chemistry 2024

Open Access Article. Published on 11 Oktober 2024. Downloaded on 07.01.26 22:54:55.
This article is licensed under a Creative Commons Attribution 3.0 Unported Licence.

distance are shown in white, while those at shorter or longer distances from the van der Waals radii are displayed in red and blue, respectively. In contrast to tartaric acid molecules,[92] with numerous intensely red spots, distributed throughout the surface, which confirmed the presence of an extensive hydrogen bond network (Fig. 6), on the surface of C_{12}_TA_C_{12} and C_{18}_TA_C_{18}, a significant number of white regions were observed, corresponding to van der Waals interactions. In unmodified tartaric acid, both hydroxyl and carboxyl groups formed strong H-bonds, as indicated by the intense red spots. In turn, in the tartaric acid-derived esters, the red spots present on the hydroxyl groups were much more intense than those located on the carbonyl groups. This observation supports the much weaker character of the H-bonds formed by the C═O group, resulting from their much longer distances, as discussed in the previous section. This plot can be decomposed into atoms involved in specific interactions and their relative percentage contributions (Fig. 6).

To calculate the percentage contribution of specific interactions, a two-dimensional fingerprint plot was generated. In C_{12}_TA_C_{12}, the hydrogen bonds (depicted as long, slender spikes) made up 15% of the total Hirshfeld surface (Fig. S32†). The great majority (83%) constituted H···H interactions, observed as a characteristic area between the spikes. In the case of C_{18}_TA_C_{18}, hydrogen bonds make up 11% of the interactions, while H···H interactions account for almost 88% (Fig. S33†). This is not surprising considering the longer alkyl chains present in the structure. Additionally, the highlighted red area in the middle of the fingerprint plot is more intense in the case of the ester with a longer alkyl chain, indicating that a substantial fraction of points on the Hirshfeld surfaces consisted of closely aligned H···H contacts between the long *n*-alkyl chains (*i.e.*, almost linear orientation between adjacent molecules).

This leads to a significant number of dispersive interactions.[94,95] For unmodified tartaric acid, the percentage contribution of specific interactions was the opposite. The H···O/O···H interactions constituted as much as 71%, while the H···H interactions accounted for 15% (Fig. S31†). The lighter blue color of the spikes in the TA histogram compared to those in the ester derivative indicated a more frequent occurrence of hydrogen interactions in the unmodified tartaric acid crystal structure. The examination of both the precursor and one of the diesters facilitated the discernment of distinct patterns. Through an analysis of enthalpy changes within the compound series, we speculate that further chain extension is unlikely to exert a pronounced impact on the distribution of hydrogen bonds, although it may influence their intensity.

Biodegradability

The ultimate biodegradability (*i.e.*, complete mineralization to CO_2, H_2O, and microbial biomass) was tested at concentrations of approximately 15 mg L^{-1}. C_{12}_TA_C_{12} (78%) and C_{16}_TA_C_{16} (38%) showed appreciable degradation (Fig. 7a). None of these compounds could be considered readily biodegradable (at least 60% degradation within a 10-day window, starting when the degradation reaches 10%),[61] yet C_{12}_TA_C_{12} was close to the threshold (a degradability window of 12.2 days). All the other compounds showed degradability within the error of the measurement. Considering structure–biodegradability relationships, the tested diesters do not possess fragments that would make them resistant to degradation (*e.g.*, branching and presence of halogen atoms); in contrast, the straight alkyl chains found in their structure are usually readily degradable.[96] Nevertheless, if such alkyl chains are too long, they can exhibit considerable microbial toxicity.[97] It is, therefore, possible that some of the diesters were not degraded, not because they were recalcitrant but because the

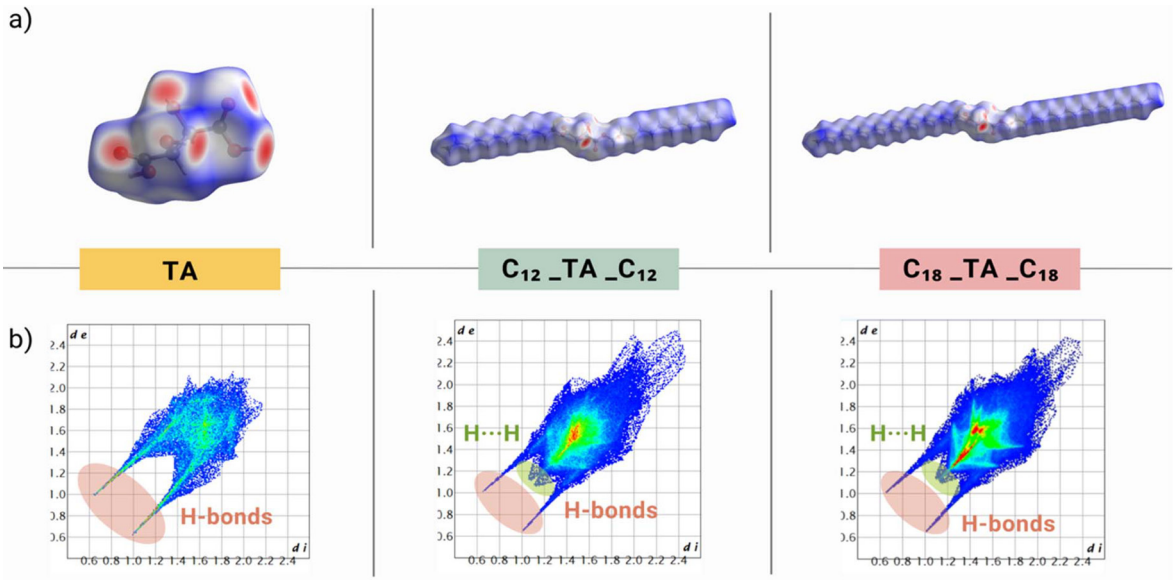

Fig. 6 (a) 3D Hirshfeld surface area and (b) 2D Hirshfeld fingerprint plots of TA, C_{12}_TA_C_{12} and C_{18}_TA_C_{18}.

Open Access Article. Published on 11 Oktober 2024. Downloaded on 07.01.26 22:54:55.
This article is licensed under a Creative Commons Attribution 3.0 Unported Licence.

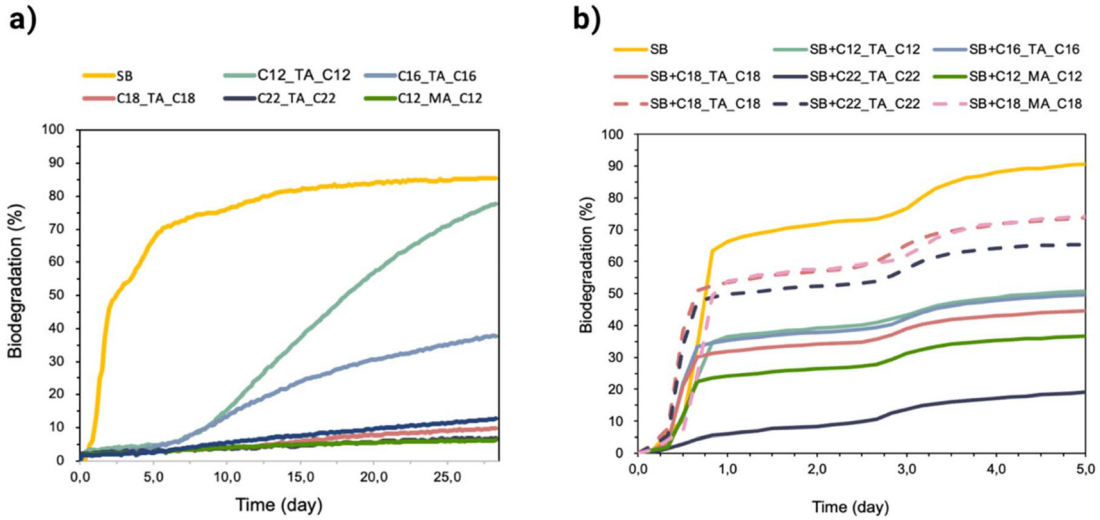

Fig. 7 (a) Ultimate biodegradation of tartaric and mucic acid diesters. SB: sodium benzoate (positive control), (b) toxicity of tartaric acid diesters (C_{12}_TA_C_{12}, C_{16}_TA_C_{16}, C_{18}_TA_C_{18}, and C_{22}_TA_C_{22}) and mucic acid diesters (C_{12}_MA_C_{12} and C_{18}_MA_C_{18}) to microbial inoculum. Solid lines represent the biodegradation of SB in the presence of diesters at concentrations of approximately 15 mg L^{-1}, while dashed lines show tests conducted at diester concentrations of approximately 4 mg L^{-1}.

concentrations used in the test were too high and inhibited the activity of microbial inoculum. Concentrations in the mg L^{-1} range are unlikely to occur in the environment (organic trace pollutants are present in surface water in concentrations of ng L^{-1} to μg L^{-1}); consequently, toxic inhibition of microorganisms is also unlikely.[98] Unfortunately, the respirometric method does not allow for testing lower concentrations; however, we could examine if toxic inhibition indeed occurred in our test or not. To this end, we conducted another test in which easily degradable sodium benzoate was added to all the samples containing diesters and the degradation of sodium benzoate was followed for 5 days (since within this time, sodium benzoate reached over 60% degradation, but none of diesters did so).

Indeed, all the diesters inhibited the activity of the microbial inoculum, as shown by the biodegradation of sodium benzoate tested alone being higher than its biodegradation in the presence of diesters (Fig. 7). As expected, both longer diester alkyl chains and higher diester concentrations gave a greater degree of inhibition. Interestingly, the didodecyl substituted ester of mucic acid (C_{12}_MA_C_{12}) was more toxic toward the inoculum than the ester of tartaric acid having the same substituents (C_{12}_TA_C_{12}, Fig. 7a) when tested at concentrations of 15 mg L^{-1}, which might explain why the latter was highly degraded, but the former was not (Fig. 7b). Considering that homologs having short alkyl chains are degradable to a great extent (despite showing some degree of inoculum inhibition) and that long chain homologs showed considerable inhibition of the inoculum (at 15 mg L^{-1}), it can be expected that the latter are also degradable if tested at lower, non-inhibitory concentrations. However, more detailed tests at lower concentrations would be required to confirm this hypothesis (*e.g.*, OECD 309 biodegradation simulation test).[99]

Conclusions

A new group of sustainable materials with physical properties suitable for application as PCMs have been developed using renewable, inexpensive precursors. Sugar acid-derived esters showed very high enthalpies of fusion, from 133 up to 221 J g^{-1} ± 5%, and T_m values ranging from 67 to 137 °C ± 2 °C, suitable for low-cost TES. Increasing the number of hydroxyl groups in the molecule improved thermal properties but reduced stability, except for a tartaric acid derivative that remained stable over 500 heating/cooling cycles. This hypothesis, however, would need to be tested on samples with more OH groups.

In addition to their sustainability, confirmed by green chemistry metrics, the materials are not expected to be persistent in the environment. Tartaric acid esterified with dodecyl chains showed high biodegradability (slightly below the readily biodegradable criterion), while the hexadecyl homolog showed lower biodegradability. Higher homologs were not degraded, likely due to the high test concentrations inhibiting microbial activity. However, at environmentally realistic concentrations (at least three orders of magnitude lower), toxic inhibition is not expected, and the biodegradability of larger homologs may be higher. These bioderived PCMs show promise for sustainable thermal energy storage applications, balancing hydrogen bonding and van der Waals interactions to tune physical properties.

Author contributions

Conceptualization: M. G., K. M., and A. B.-S., data curation: M. G., formal analysis: M. G. and A. B.-S., funding acquisition:

 This journal is © The Royal Society of Chemistry 2024

M. G. and A. B.-S., investigation: M. G. and M. M., methodology: M. G., M. M., K. M., and A. B.-S., visualization: M. G., writing – original draft: M. G., A. B.-S., and S. S. and writing – review & editing: A. C., D. T., and K. M.

Data availability

The data supporting this article have been included as part of the ESI. Crystallographic data for C_{12}_TA_C_{12} and C_{18}_TA_C_{18} have been deposited at the Cambridge Structural Database, such as CCDC 2369962 and 2369963.†

Conflicts of interest

There are no conflicts to declare.

Acknowledgements

M. G., A. B.-S., and K. M. acknowledge the Polish National Agency for Academic Exchange under the Strategic Partnerships programme (BPI/PST/2021/1/00039)., A. B.-S. acknowledges the Excellence Initiative – Research University Programme under Grant No. 04/050/SDU/10-21-01, Rector's Pro-quality Grant, Silesian University of Technology 04/050/RGJ23/0168 and the habilitation grant 04/050/RGH22/0162. M. G. acknowledges the Silesian University of Technology (04/050/BKM24/0196). The contributions of Mr Szymon Ruczka and Dr Anna Kolanowska are appreciated.

This research was undertaken using the MX2 beamline at the Australian Synchrotron, part of ANSTO, and made use of the Australian Cancer Research Foundation (ACRF) detector.

References

1 A. A. Mehrizi, H. Karimi-Maleh, M. Naddafi and F. Karimi, *J. Energy Storage*, 2023, **61**, 106859.
2 I. Energy Agency, *Net Zero by 2050 - A Roadmap for the Global Energy Sector*, 2050.
3 N. Soodoo, K. D. Poopalam, L. Bouzidi and S. S. Narine, *J. Energy Storage*, 2022, **51**, 104355.
4 A. Stamatiou, M. Obermeyer, L. J. Fischer, P. Schuetz and J. Worlitschek, *Renewable Energy*, 2017, **108**, 401–409.
5 S. L. Piper, C. M. Forsyth, M. Kar, C. Gassner, R. Vijayaraghavan, S. Mahadevan, K. Matuszek, J. M. Pringle and D. R. MacFarlane, *RSC Sustainability*, 2023, 207890.
6 K. Matuszek, R. Vijayaraghavan, M. Kar and D. R. Macfarlane, *Cryst. Growth Des.*, 2020, **20**, 1285–1291.
7 Y. Yuan, N. Zhang, W. Tao, X. Cao and Y. He, *Renewable Sustainable Energy Rev.*, 2014, **29**, 482–498.
8 K. Matuszek, S. L. Piper, A. Brzęczek-Szafran, B. Roy, S. Saher, J. M. Pringle and D. R. Macfarlane, *Adv. Mater.*, 2024, **36**, 23.
9 S. L. Piper, C. M. Forsyth, M. Kar, C. Gassner, R. Vijayaraghavan, S. Mahadevan, K. Matuszek, J. M. Pringle and D. R. MacFarlane, *RSC Sustainability*, 2023, **1**, 470–480.
10 K. Du, J. Calautit, Z. Wang, Y. Wu and H. Liu, *Appl. Energy*, 2018, **220**, 242–273.
11 J. F. Hinojosa, S. F. Moreno and V. M. Maytorena, *Energies*, 2023, **16**(7), 3078.
12 D. Cabaleiro, F. Agresti, S. Barison, M. A. Marcos, J. I. Prado, S. Rossi, S. Bobbo and L. Fedele, *Appl. Therm. Eng.*, 2019, **159**, 113868.
13 D. Patel, W. Wei, H. Singh, K. Xu, C. Beck, M. Wildy, J. Schossig, X. Hu, D. C Hyun, W. Chen and P. Lu, *ACS Sustainable Chem. Eng.*, 2023, **11**, 11570–11579.
14 A. E. Kabeel, A. Khalil, S. M. Shalaby and M. E. Zayed, *Energy Convers. Manage.*, 2016, **113**, 264–272.
15 M. Faegh and M. B. Shafii, *Desalination*, 2017, **409**, 128–135.
16 R. Padovan and M. Manzan, *Sol. Energy*, 2014, **103**, 563–573.
17 Q. Al-Yasiri and M. Szabó, *J. Build. Eng.*, 2021, **36**, 102122.
18 F. Souayfane, F. Fardoun and P. H. Biwole, *Energy Build.*, 2016, **129**, 396–431.
19 X. Wang, W. Li, Z. Luo, K. Wang and S. P. Shah, *Energy Build.*, 2022, **260**, 111923.
20 M. C. Floros and S. S. Narine, *Energy*, 2016, **115**, 924–930.
21 H. Mehling and M. A. White, *Chem. Phys. Impact.*, 2023, **6**, 100222.
22 N. R. Jankowski and F. P. McCluskey, *Appl. Energy*, 2014, **113**, 1525–1561.
23 Q. Zhang, H. Yan, Z. Zhang, J. Luo, N. Yin, Z. Tan and Q. Shi, *Mater. Today Sustain.*, 2021, **11–12**, 100064.
24 S. Kahwaji and M. A. White, *Molecules*, 2021, **26**, 21.
25 D. Rozanna, T. G. Chuah, A. Salmiah, T. S. Y. Choong and M. Sa'ari, *Int. J. Green Energy*, 2005, **1**, 495–513.
26 J. C. Van Miltenburg, H. A. J. Oonk and L. Ventola, *J. Chem. Eng. Data*, 2001, **46**, 90–97.
27 W. Acree and J. S. Chickos, *J. Phys. Chem. Ref. Data*, 2017, **46**, 1.
28 R. Ravotti, O. Fellmann, N. Lardon, L. J. Fischer, A. Stamatiou and J. Worlitschek, *Appl. Sci.*, 2019, **9**, 2.
29 H. Fatahi, J. Claverie and S. Poncet, *Appl. Sci.*, 2022, **12**(23), 12019.
30 L. Raghunanan, M. C. Floros and S. S. Narine, *Thermochim. Acta*, 2016, **644**, 61–68.
31 H. Nazir, M. Batool, F. J. Bolivar Osorio, M. Isaza-Ruiz, X. Xu, K. Vignarooban, P. Phelan, Inamuddin and A. M. Kannan, *Int. J. Heat Mass Transfer*, 2019, **129**, 491–523.
32 D. Feldman, D. Banu and D. Hawes, *Sol. Energy Mater. Sol. Cells*, 1995, **36**, 311–322.
33 A. A Aydin, *Sol. Energy Mater. Sol. Cells*, 2013, **113**, 44–51.
34 A. A. Aydin and H. Okutan, *Sol. Energy Mater. Sol. Cells*, 2011, **95**, 2417–2423.
35 A. A. Aydin and A. Aydin, *Sol. Energy Mater. Sol. Cells*, 2012, **96**, 93–100.

Open Access Article. Published on 11 Oktober 2024. Downloaded on 07.01.26 22:54:55.
This article is licensed under a Creative Commons Attribution 3.0 Unported Licence.

Open Access Article. Published on 11 Oktober 2024. Downloaded on 07.01.26 22:54:55.
This article is licensed under a Creative Commons Attribution 3.0 Unported Licence.

36 A. Sari, A. Biçer and A. Karaipekli, *Mater. Lett.*, 2009, **63**, 1213–1216.
37 A. Stamatiou, M. Obermeyer, L. J. Fischer, P. Schuetz and J. Worlitschek, *Renewable Energy*, 2017, **108**, 401–409.
38 Ö. Kaplan, N. G Tosun, İ. Gökçe and C. Alkan, *Energy Sources, Part A*, 2023, **45**, 608–622.
39 R. Ravotti, O. Fellmann, N. Lardon, L. J. Fischer, A. Stamatiou and J. Worlitschek, *Appl. Sci.*, 2018, **8**, 7.
40 E. P. del Barrio, A. Godin, M. Duquesne, J. Daranlot, J. Jolly, W. Alshaer, T. Kouadio and A. Sommier, *Sol. Energy Mater. Sol. Cells*, 2017, **159**, 560–569.
41 A. Solé, H. Neumann, S. Niedermaier, I. Martorell, P. Schossig and L. F. Cabeza, *Sol. Energy Mater. Sol. Cells*, 2014, **126**, 125–134.
42 C. Barreneche, A. Gil, F. Sheth, A. I Fernández and L. F. Cabeza, *Sol. Energy*, 2013, **94**, 344–351.
43 A. Kaizawa, N. Maruoka, A. Kawai, H. Kamano, T. Jozuka, T. Senda and T. Akiyama, *Heat Mass Transfer*, 2008, **44**, 763–769.
44 A. Sari, A. Biçer and A. Karaipekli, *Mater. Lett.*, 2009, **63**, 1213–1216.
45 A. Sari, R. Eroglu, A. Biçer and A. Karaipekli, *Chem. Eng. Technol.*, 2011, **34**, 87–92.
46 A. Biçer and A. Sar, *Sol. Energy Mater. Sol. Cells*, 2012, **102**, 125–130.
47 A. Sari, *Energy Convers. Manage.*, 2012, **64**, 68–78.
48 A. Sari and A. Biçer, *Sol. Energy Mater. Sol. Cells*, 2012, **101**, 114–122.
49 S. H. Yalkowsky and D. Alantary, *J. Pharm. Sci.*, 2018, **107**, 1211–1227.
50 S. L. Piper, C. M. Forsyth, M. Kar, D. R. MacFarlane, K. Matuszek and J. M. Pringle, *Mater. Adv.*, 2021, **2**, 7650–7661.
51 K. D. Poopalam, L. Raghunanan, L. Bouzidi, S. K. Yeong and S. S. Narine, *Sol. Energy Mater. Sol. Cells*, 2019, **201**, DOI: 10.1002/er.4711.
52 T. Inagaki and T. Ishida, *J. Phys. Chem. C*, 2016, **120**, 7903–7915.
53 B. Gaida, J. Kondratowicz, S. L. Piper, C. M. Forsyth, A. Chrobok, D. R. Macfarlane, K. Matuszek and A. Brzeczek-Szafran, *ACS Sustainable Chem. Eng.*, 2024, **12**, 623–632.
54 N. Biedermann, J. Schnizer, D. Lager, M. Schnürch and C. Stanetty, *J. Org. Chem.*, 2024, **89**(8), 5573–5588.
55 D. Aragão, J. Aishima, H. Cherukuvada, R. Clarken, M. Clift, N. P. Cowieson, D. J. Ericsson, C. L. Gee, S. Macedo, N. Mudie, S. Panjikar, J. R. Price, A. Riboldi-Tunnicliffe, R. Rostan, R. Williamson and T. T. Caradoc-Davies, *J. Synchrotron Radiat.*, 2018, **25**, 885–891.
56 T. M. McPhillips, S. E. McPhillips, H. J. Chiu, A. E. Cohen, A. M. Deacon, P. J. Ellis, E. Garman, A. Gonzalez, N. K. Sauter, R. P. Phizackerley, S. M. Soltis and P. Kuhn, *J. Synchrotron Radiat.*, 2002, **9**, 401–406.
57 W. Kabsch, *J. Appl. Crystallogr.*, 1993, **26**, 795–800.
58 G. M. Sheldrick, *Acta Crystallogr., Sect. C: Struct. Chem.*, 2015, **71**, 3–8.
59 G. M. Sheldrick, *Acta Crystallogr., Sect. A: Found. Adv.*, 2015, **71**, 3–8.
60 O. V. Dolomanov, L. J. Bourhis, R. J. Gildea, J. A. K. Howard and H. Puschmann, *J. Appl. Crystallogr.*, 2009, **42**, 339–341.
61 OECD, *Test No. 301: Ready Biodegradability*, OECD Publishing, 1992, 301.
62 K. Izawa, Y. Amino, M. Kohmura, Y. Ueda and M. Kuroda, *Comprehensive Natural Products II: Chemistry and Biology*, 2010, vol. 4, pp. 631–671.
63 Y. Ukaji and T. Soeta, *Compr. Chirality*, 2012, **3**, 176–201.
64 I. Goldberg and J. S. Rokem, *Encyclopedia of Microbiology*, 3rd edn, 2009, pp. 421–442.
65 E. Anet and T. Reynolds, *Nature*, 1954, **174**, 930.
66 R. Sakuta and N. Nakamura, *Int. J. Mol. Sci.*, 2019, 20.
67 D. Barth and M. G. Wiebe, *Appl. Microbiol. Biotechnol.*, 2017, **101**, 4033–4040.
68 D. Mojzita, M. Wiebe, S. Hilditch, H. Boer, M. Penttilä and P. Richard, *Appl. Environ. Microbiol.*, 2010, **76**, 169–175.
69 D. Concha, K. Rodríguez-Núñez, L. Castillo, R. Martínez and C. Bernal, *Biochem. Eng. J.*, 2022, **187**, 108646.
70 O. Okogeri and V. N. Stathopoulos, *Int. J. Thermofluids*, 2021, **10**, 100081.
71 P. Munkajohnpong, C. Kesornpun, S. Buttranon, J. Jaroensuk, N. Weeranoppanant and P. Chaiyen, *Biofuels, Bioprod. Biorefin.*, 2020, **14**, 986–1009.
72 A. Krishnan, B. McNeil and D. Stuart, *Front. Bioeng. Biotechnol.*, 2020, **8**, 610936.
73 C. R. Mcelroy, A. Constantinou, L. C. Jones, L. Summerton and J. H. Clark, *Green Chem.*, 2015, **17**, 3111.
74 K. D. Poopalam, L. Raghunanan, L. Bouzidi, K. Y. Shoot and S. Narine, *Int. J. Energy Res.*, 2019, **43**, 13.
75 R. Ravotti, J. Worlitschek, C. R. Pulham and A. Stamatiou, *Molecules*, 2020, **25**(23), 5572.
76 K. Matuszek, M. Kar, J. M. Pringle and D. R. Macfarlane, *Chem Rev.*, 2023, **123**(1), 491–514.
77 T. Inagaki and T. Ishida, *J. Am. Chem. Soc.*, 2016, **138**, 11810–11819.
78 S. Cabus, K. Bogaerts, J. Van Mechelen, M. Smet and B. Goderis, *Cryst. Growth Des.*, 2013, **13**, 3438–3446.
79 S. Petit, R. Ralainirina, S. Favre, R. D. Baynast, *WO. Pat.*, 1993002039A1, 1993.
80 W. Wei, F. Feng, B. Perez, M. Dong and Z. Guo, *Green Chem.*, 2015, **17**, 3475–3489.
81 Y. Liu, Y. Deng, J. Zheng, F. Wu, J. Lu, S. Sun, D. Wu and T. Wu, *Sol. Energy Mater. Sol. Cells*, 2022, 248.
82 S. J. Grabowski, W. A. Sokalski and J. Leszczynski, *Chem. Phys.*, 2007, **337**, 68–76.
83 T. Kondo and C. Sawatari, *Polymer*, 1996, **37**, 393–399.
84 R. N. A. H. Lewis and R. N. McElhaney, *Biochim. Biophys. Acta, Biomembr.*, 2013, **1828**, 2347–2358.
85 L. Hunger, L. Al-Sheakh, D. H. Zaitsau, S. P. Verevkin, A. Appelhagen, A. Villinger and R. Ludwig, *Chem. – Eur. J.*, 2022, **28**, 46.
86 M. S. Cintrón and D. J. Hinchliffe, *Fibers*, 2015, **3**, 30–40.
87 A. Yamaguchi, N. Hiyoshi, O. Sato and M. Shirai, *Green Chem.*, 2011, **13**, 873–881.

This journal is © The Royal Society of Chemistry 2024

Open Access Article. Published on 11 Oktober 2024. Downloaded on 07.01.26 22:54:55.
This article is licensed under a Creative Commons Attribution 3.0 Unported Licence.

88 T. K. Harris and A. S. Mildvan, *Proteines – Structure, Function, Bioinformation*, 1999, **35**, 275–282.
89 L. Jiang and L. Lai, *J. Biol. Chem.*, 2002, **277**, 37732–37740.
90 T. Steiner, *Crystallogr. Rev.*, 2003, **9**, 177–228.
91 Y. Liu, Y. Deng, J. Zheng, F. Wu, J. Lu, S. Sun, D. Wu and T. Wu, *Sol. Energy Mater. Sol. Cells*, 2022, **248**, 112031.
92 D. Mroz, R. Wang, U. Englert and R. Dronskowski, *CrystEngComm*, 2021, **23**, 1052–1058.
93 M. A. Spackman and D. Jayatilaka, *CrystEngComm*, 2009, **11**, 19–32.
94 S. J. Prathapa, C. Slabbert, M. A. Fernandes and A. Lemmerer, *CrystEngComm*, 2019, **21**, 41–52.
95 M. A. Spackman and J. J. McKinnon, *CrystEngComm*, 2002, **4**, 378–392.
96 R. S. Boethling, E. Sommer and D. DiFiore, *Chem. Rev.*, 2007, **107**, 2167–2820.
97 M. Markiewicz, M. Piszora, N. Caicedo, C. Jungnickel and S. Stolte, *Water Res.*, 2013, **47**(9), 2921–2928.
98 J. C. G. Sousa, A. R. Ribeiro, M. O. Barbosa, M. F. R. Pereira and A. M. T. Silva, *J. Hazard. Mater.*, 2018, **344**, 146–162.
99 OECD, *Guidelines for testing of chemicals 309: Aerobic mineralisation in serface water - Simulation biodegradation test*, 2004.